RESEARCH ARTICLE

Direct observation of negative cooperativity in a detoxification enzyme at the atomic level by Electron Paramagnetic Resonance spectroscopy and simulation

Xiaowei Bogetti[1] | Anthony Bogetti[1] | Joshua Casto[1] | Gordon Rule[2] |
Lillian Chong[1] | Sunil Saxena[1]

[1]Department of Chemistry, University of Pittsburgh, Pittsburgh, Pennsylvania, USA

[2]Department of Biological Sciences, Carnegie Mellon University, Pittsburgh, Pennsylvania, USA

Correspondence
Lillian Chong, Department of Chemistry, University of Pittsburgh, Pittsburgh, PA 15260, USA.
Email: ltchong@pitt.edu

Sunil Saxena, Department of Chemistry, University of Pittsburgh, Pittsburgh, PA 15260, USA.
Email: sksaxena@pitt.edu

Review Editor: John Kuriyan

Abstract

The catalytic activity of human glutathione S-transferase A1-1 (hGSTA1-1), a homodimeric detoxification enzyme, is dependent on the conformational dynamics of a key C-terminal helix α9 in each monomer. However, the structural details of how the two monomers interact upon binding of substrates is not well understood and the structure of the ligand-free state of the hGSTA1-1 homodimer has not been resolved. Here, we used a combination of electron paramagnetic resonance (EPR) distance measurements and weighted ensemble (WE) simulations to characterize the conformational ensemble of the ligand-free state at the atomic level. EPR measurements reveal a broad distance distribution between a pair of Cu(II) labels in the ligand-free state that gradually shifts and narrows as a function of increasing ligand concentration. These shifts suggest changes in the relative positioning of the two α9 helices upon ligand binding. WE simulations generated unbiased pathways for the seconds-timescale transition between alternate states of the enzyme, leading to the generation of atomically detailed structures of the ligand-free state. Notably, the simulations provide direct observations of negative cooperativity between the monomers of hGSTA1-1, which involve the mutually exclusive docking of α9 in each monomer as a lid over the active site. We identify key interactions between residues that lead to this negative cooperativity. Negative cooperativity may be essential for interaction of hGSTA1-1 with a wide variety of toxic substrates and their subsequent neutralization. More broadly, this work demonstrates the power of integrating EPR distances with WE rare-events sampling strategy to gain mechanistic information on protein function at the atomic level.

KEYWORDS
DEER, detoxification enzyme, Enhanced sampling MD, GST, protein dynamics

1 | INTRODUCTION

Glutathione S-transferases (GSTs) are a family of detoxification enzymes found in many organisms. Human GST A1-1 (hGSTA1-1) is a homodimer, with each monomer containing an active site that deactivates cellular toxins in cells by conjugating the toxins to glutathione (Armstrong, 1997; Hayes & Pulford, 1995). There is much evidence that hGSTA1-1 exists in a large ensemble of states (Honaker et al., 2013; Pettersson et al., 2017). The structure of the S-hexylglutathione (GSHex)-bound hGSTA1-1 has previously been solved by x-ray crystallography and is shown in Figure 1a (Le Trong et al., 2002). In this ligand-bound structure, the C-terminal α9 helix of each monomer (highlighted in blue in Figure 1a and labeled as α9$_A$ and α9$_B$ respectively, for monomers A and B) functions as a "lid" over the corresponding active/binding site. This helix plays an essential role in the catalytic function of the dimer. Mutations of highly conserved sites at the α9 helix significantly decrease the catalytic efficiency of hGSTA1-1 (Gustafsson & Mannervik, 1999; Nilsson et al., 2002). In addition, the protein is nonfunctional in the absence of this helix (Dirr & Wallace, 1999). There are two main types of interactions that are present at the interface of the hGSTA1-1 dimer and the α9 helix. The highly conserved Tyr9, Phe10 (interface), and Phe220 (at α9 helix) residues form an aromatic cluster in the ligand-bound structure (Cameron et al., 1995; Ibarra et al., 2001). Hydrophobic interactions between Tyr9/Phe10 and Phe220 are believed to lock α9 over the active site (Nilsson et al., 2002). In addition, the salt bridge between the conserved Asp42 (α2 helix, which

is adjacent to α9) and Arg221 (right after the α9 helix) residues is believed to affix the α9 helix as a lid over the active sites and may be important for inactivating cellular toxins (Widersten et al., 1996).

However, the entire structure of ligand-free hGSTA1-1 has yet to be resolved. In the available structure of the ligand-free hGSTA1-1 dimer, shown in Figure 1b, the α9 helix of each monomer is largely missing (Grahn et al., 2006), which has left unanswered questions about the relation of the structure and dynamics to function for this critical helix. There are conflicting hypotheses about the structure of the α9 region in the ligand-free state. Some reports suggest that the α9 region is disordered (Cameron et al., 1995; Le Trong et al., 2002), while others suggest that the region is helical (Grahn et al., 2006; Nilsson et al., 2002; Zhan & Rule, 2004), but delocalized (i.e., undocked) with respect to the binding sites (Nieslanik et al., 2001; Pettersson et al., 2017). In addition, knowledge of the full α9 conformational ensemble in the ligand-free state, as well as information on how the two monomers interact, is essential to fully understand the atomic-level structural details and function for this enzyme.

Here, we characterize the ligand-free conformational ensemble of the hGSTA1-1 enzyme in atomistic detail using a combination of pulsed EPR distance measurements and weighted ensemble (WE) molecular dynamics (MD) simulations. Pulsed EPR distance measurements (Bonora et al., 2004; Borbat & Freed, 1999; Jeschke et al., 2000; Kulik et al., 2001; Milikisyants et al., 2009; Milov et al., 1998; Pannier et al., 2011), generally enabled by site-directed spin labeling, are powerful probes for
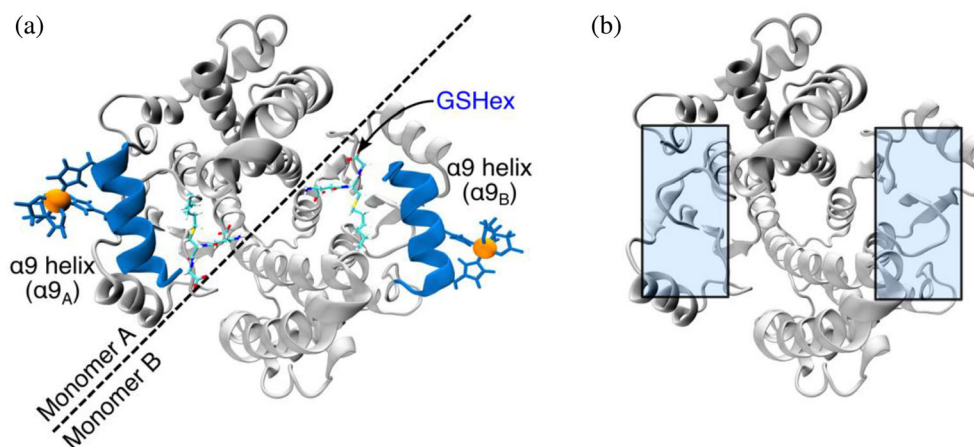
FIGURE 1 (a) Crystal structure of S-hexylglutathione (GSHex)-bound human glutathione S-transferase A1-1 (PDB: 1K3L). The ligand GSHex is highlighted in cyan. The α9 helices at the C-termini are highlighted in blue. The double histidine–Cu(II)–nitrilotriacetic acid EPR labels (blue sticks with the Cu(II) atoms represented as orange spheres) are introduced to the α9 helix to capture the change in the distance distribution between the labels upon introducing different concentrations of GSHex. (b) In the absence of a ligand, the structure of the α9 helices is unresolved (PDB: 1PKZ). The blue boxes highlight where the α9 helices are in the GSHex-bound structure.

protein–protein (Nyenhuis et al., 2020; Park et al., 2006; Schmidt et al., 2019) and protein–nucleic acid (Krumkacheva et al., 2019; Stone et al., 2008) interactions, metal and ligand binding sites (Abdullin et al., 2015; Gamble Jarvi et al., 2019; Yin et al., 2017), and macromolecular conformational changes (Altenbach et al., 2008; Barth et al., 2018; Dalmas et al., 2014; Dastvan et al., 2019; Evans et al., 2016; Evans et al., 2020; Hett et al., 2021; Kear et al., 2009; Schmidt et al., 2022; Stewart et al., 2022). Such measurements can also be performed *in cells* (Igarashi et al., 2010; Joseph et al., 2015; Martorana et al., 2014; Meichsner et al., 2021; Roser et al., 2016; Teucher et al., 2019). In this work, we employ a Cu(II)-based protein labeling scheme, which involves the strategic placement of two histidine residues (double histidine [dHis]) to allow rigid chelation to a Cu(II) complex. In addition, the introduction of the Cu(II) in complex with the chelating agent, such as iminodiacetic acid (Lawless et al., 2017) or nitrilotriacetic acid (NTA) (Ghosh et al., 2018), increases the specificity of Cu(II) binding to dHis sites and avoids nonspecific binding of Cu(II) to elsewhere in the protein. The dHis–Cu(II) protein labels are incisive probes of protein conformational change, since the dHis–Cu(II) based distance measurements can yield distance distributions that are up to five times narrower compared to commonly used nitroxide labels (Cunningham et al., 2015). We performed such distance measurements on several ligands, all of which suggested a restriction of the conformational space occupied by the α9 helices of hGSTA1-1 in the presence of ligand. In addition, the data showed a change in the positioning of the two helices. Based on this insight, we exploited MD simulations to gain knowledge on slow conformational dynamics. To enable simulation of the seconds-timescale transition between alternate states of hGSTA1-1, we applied the WE path sampling strategy (Huber & Kim, 1996; Zuckerman & Chong, 2017). The WE strategy has been demonstrated to be orders of magnitude more efficient in generating pathways and rate constants for rare events such as protein–protein binding on the multi-microsecond timescale (Saglam & Chong, 2019) and the large-scale opening of the coronavirus spike protein on the seconds timescale (Dommer et al., 2023). Computational strategies have been able to use EPR data to predict distance distributions (MMM [Jeschke, 2018], double electron–electron resonance [DEER]-PREdict [Tesei et al., 2021], ensemble-biased metadynamics [Marinelli & Faraldo-Gómez, 2015]) and predict or refine protein structures (MELD [MacCallum et al., 2015], restrained ensemble MD [Islam et al., 2013], RosettaEPR [Hirst et al., 2011]). In this work, we demonstrate how the WE strategy can use EPR data as a guide to focus simulation on transitions, providing continuous pathways without applying any biasing forces.

2 | MATERIALS AND METHODS

2.1 | Protein purification and sample preparation

For the EPR experiments, we mutated Lys211 and Glu215 in the α9 helix of each monomer to histidines. The Cu(II)–NTA complex was then attached to this dHis site. As shown in previous work (Lawless et al., 2018), the Lys211His and Glu215His mutations do not perturb the enzyme activity. The Lys211His/Glu215His mutant was expressed in Luria broth and purified based on the previously described protocol (Singewald et al., 2020). The ligand GSHex was purchased from Sigma Aldrich. The synthesis of ethacrynic acid glutathione conjugate (EASG) and S-(2,4-dinitrophenyl)glutathione (GS-DNB) were based on the previously published protocols (Ploemen et al., 1990; Schramm et al., 1984). As hGSTA1-1 is a homodimer, a dHis mutant provides two Cu(II)–NTA labeling sites. The purified protein was concentrated, aliquoted to ~220 μM in sodium phosphate buffer (pH = 6.5, 50 mM sodium phosphate and 150 mM NaCl) and stored at −80°C.

All samples for EPR measurements were prepared based on the protocol described in previous work (Gamble Jarvi et al., 2020; Ghosh et al., 2018; Singewald et al., 2021). Briefly a 10 mM stock solution of Cu(II)–NTA and a 3-N-morpholinopropanesulfonic acid (MOPS) buffer (pH = 7.4, 50 mM MOPS, 100 mM NaCl in D_2O) were prepared (Gamble Jarvi et al., 2020). The Cu(II)-labeling can be performed in a variety of buffer (Gamble Jarvi et al., 2020), and over a range of pH (Wort, Arya, et al., 2021), to provide sensitive (Ackermann et al., 2021) measurements of a wide range of biophysical information (Gamble Jarvi et al., 2018, 2019; Oranges et al., 2022; Sameach et al., 2019; Singewald et al., 2020).

The hGSTA1-1 samples contained 100 μM hGSTA1-1 dimer, 200 μM Cu(II)–NTA, and a GSHex concentration of 0, 50, 100, 150, 200, and 400 μM. Samples containing the EASG and GS-DNB ligands were prepared with a ligand concentration of 1 mM to ensure all active sites are saturated with ligands. The apparent dissociation constant (K_D) of hGSTA1-1 to GSHex has been determined in previous work to be 70 nM (Kuhnert et al., 2005). Although the binding affinities of the EASG and GS-DNB ligand have not been determined, we expect sub-micromolar affinity of these ligands due to their hydrophobic nature. Thus, given the concentration of the hGSTA1-1 protein relative to the K_D values, stoichiometric binding of the ligand to the binding sites is expected until all hGSTA1-1 is fully loaded with ligands. The sample used for a biological repeat was prepared with 400 μM hGSTA1-1 dimer and 800 μM Cu(II)–NTA. All EPR samples were incubated at 4°C for 35 min to achieve

maximum binding efficiency of Cu(II)–NTA before 40% (v/v) D_6- glycerol was added as a cryoprotectant. All samples were placed in quartz tubes with ID = 2 mm and OD = 3 mm and were flash frozen using liquid MAP-Pro propylene/propane gas. A detailed protocol for dHis–Cu (II) sample preparation has been published elsewhere (Singewald et al., 2021). For each sample, proper binding of dHis site to Cu(II)–NTA are verified through continuous wave-EPR (CW-EPR) and electron spin echo envelope modulation (ESEEM) (Mims, 1972a, 1972b) experiments. More details of the CW-EPR and ESEEM results are available in the Supporting Information and Figures S1–S3.

2.2 | EPR distance measurements

To determine the distance distribution between EPR labels within hGSTA1-1, four-pulse DEER experiments (Pannier et al., 2011) were performed at 18 K and at Q-band frequency. The measurements were performed with a Bruker ElexSys E580 spectrometer with a Bruker ER5106-QT2 resonator and a 300 W amplifier. The dHis–Cu(II)-based DEER time-domain signal for each sample were averaged over three measurements with pump pulses at strategically selected magnetic fields. Specifically, the pump pulses were placed at 100, 580, and 827 G lower than the maximum of the field swept-electron spin echo spectrum. The three magnetic fields were chosen based on a recent work which showed that this acquisition scheme properly samples all molecular orientations (Bogetti et al., 2022). The pulse sequence used was $(\pi/2)\upsilon \quad -\tau - (\pi)\upsilon_A - \tau + t - (\pi)\upsilon_B - T - t - (\pi)\upsilon_A - T -$ echo. A 16-step phase cycling was used. The observer pulses, $(\pi/2)\upsilon_A$ and $(\pi)\upsilon_A$, were rectangular pulses with pulse lengths of 12 and 24 ns (or 10 and 20 ns), respectively. An 82 ns chirp pulse was used for the pump pulse, $(\pi)\upsilon_B$ to properly account for any short distances. The pump pulse was set with a frequency from -300 to -100 MHz relative to the observer pulses. The interval, t, was incremented by a step size of 20 ns (or 30 ns for one of the biological repeats shown in Figure S4) over 365 points (or 237 points if the step size was 30 ns). A long dipolar evolution time of $\sim$7 μs was achieved using deuterated solvent to enhance the phase memory relaxation time to over 9 μs (Figure S5) (Casto et al., 2021). DEERAnalysis21 was used to analyze the DEER results (Jeschke et al., 2006). Further experimental details (Schiemann et al., 2021), including labeling efficiency, DEER parameters, modulation depth, signal-to-noise ratio, and control experiments detecting native binding sites are provided in Tables S1–S3 and Figure S6. Labeling efficiency of Cu(II)–NTA to dHis sites in our work is

determined through CW-EPR experiments, which can also be optimized through pulsed dipolar EPR based on previous work (Wort, Ackermann, et al., 2021).

2.3 | Conventional molecular dynamics simulations

As initial explorations of hGSTA1-1 dynamics, both in its ligand-free state and bound states with one or two GSHex ligands present, we performed five 1 μs conventional molecular dynamics (cMD) simulations of each system. Heavy-atom (all atoms except hydrogen) coordinates for the protein were extracted from the GSHex-bound hGSTA1-1 crystal structure (PDB:1K3L) (Le Trong et al., 2002). The Reduce algorithm, as implemented in MolProbity (Chen et al., 2010), was used to correct Asn/Gln/His flips in the x-ray protein structure and the LeAP module of the AMBER software was used to protonate each titratable residue for neutral pH. Residues Lys211 and Glu215 were mutated to histidine residues, followed by aligning the dHis–Cu(II)–NTA complex to the dHis sites. Proper bonds were then added between the aligned dHis–Cu(II)–NTA and protein backbone to form the dHis–Cu(II)–NTA labeled hGSTA1-1. GAFF2 force field parameters (Wang et al., 2004) were used for the dHis–Cu(II)–NTA spin label, as previously developed (Bogetti et al., 2020), and for the GSHex ligand.

Each dHis–Cu(II)–NTA labeled hGSTA1-1 system was solvated in a truncated octahedral water box with crystal waters retained. The AMBER ff19SB force field (Tian et al., 2020) was used along with the optimal 3-charge, 4-point rigid water model water model (Izadi et al., 2014). The cMD simulations were performed using the pmemd module of the AMBER20 software package. Sodium chloride was added to neutralize the charge.

Each system was first energy-minimized without any restraints over 2000 steps to relieve the unfavorable interactions. The energy minimized structures were gradually heated to 298 K in the constant Number of atoms, volume, and temperature ensemble for 20 ps with restraints applied to all heavy atoms of the protein and ligands. The structures were subsequently equilibrated in the constant number of atoms, pressure, and temperature (NPT) ensemble for 1 ns using the Langevin thermostat with the same restraints on the solute. A 1-ns unrestrained equilibration in the NPT ensemble was then performed using the Monte-Carlo barostat (100 steps between volume change attempts) and a weak Langevin thermostat (collision frequency of 1 ps^{-1}) followed by the production simulations. To enable a 2 fs time step, all bonds to hydrogen were constrained to their equilibrium values using the SHAKE algorithm (Ryckaert et al., 1977).

Short-range nonbonded interactions were truncated at 10 Å and long-range electrostatics interactions were treated using the particle mesh Ewald methods with periodic boundary conditions.

2.4 | Weighted ensemble simulations

To enhance the conformational sampling of ligand-free GST, we performed WE simulations starting from the crystal structure of hGSTA1-1 (PDB:1K3L) (Le Trong et al., 2002) with the ligand in each monomer removed. The resulting structure was then solvated and equilibrated per the procedure in the preceding section before beginning WE. Unlike the cMD simulations, WE simulations focus computing power on simulating transitions between stable states rather than the stable states themselves (Huber & Kim, 1996). All WE simulations were performed with the open-source WESTPA 2.0 software package (Russo et al., 2022). WE sampling typically involves partitioning a progress coordinate into bins, followed by running multiple, short trajectories in parallel. At fixed time intervals, a resampling procedure is applied which either replicates or terminates trajectories to give a target number of trajectories per bin. During this resampling procedure, trajectory weights, which are assigned at the start of the WE simulation, are rigorously tracked such that all the weights sum to one at any given time during the simulation. For simulations starting from both α9 helices localized over the binding site, we employed a one-dimensional progress coordinate consisting of the sum of the heavy-atom (all atoms except hydrogen) root mean square deviation (RMSD) of both α9 helices (one from each monomer) after alignment on the rest of the protein dimer. To construct this coordinate, the main body of protein dimer (i.e., the gray parts of the protein in Figure 1a) was aligned, and the RMSD of the α9 helices were calculated. The more the deviation of the helix from its initial position the greater is the RMSD. This RMSD metric will be referred to as α9$_X$ RMSD, where X is either A or B for the two monomers. Thus, the one-dimensional coordinate used in this case was α9$_A$ RMSD + α9$_B$ RMSD. For the WE simulations starting from one helix delocalized, our one-dimensional progress coordinate consisted of the α9$_X$ RMSD of *only* the helix still localized over the binding site. The minimal adaptive binning scheme (Torrillo et al., 2021) was used with five evenly spaced bins between the trailing and leading trajectories; as typically done with this scheme, trailing and leading trajectories as well as a bottleneck trajectory (Torrillo et al., 2021) in the direction of increasing RMSD were each assigned to their own bins. A resampling time interval of 50 ps was used to maintain a target number of

five trajectories per bin. A total of three independent WE simulations were run.

To monitor any change in structure of the individual α9 helices, we calculated the heavy-atom RMSD of each α9 helix after alignment on its starting structure. Thus, any change in helical structure would result in an increase in RMSD. We refer to this RMSD metric as the helicity metric in the remainder of this manuscript.

3 | RESULTS AND DISCUSSION

In this work, we used a combination of DEER experiments and WE MD simulations to resolve the conformational ensemble of the ligand-free hGSTA1-1 enzyme at the atomic level. The EPR experiments focused on a Lys211His/Glu215His mutant of the enzyme, and this dHis site was labeled with the Cu(II)–NTA complex. The Lys211His and Glu215His mutations are in the α9 helix and do not perturb enzyme activity as shown in previous work (Lawless et al., 2018). Given that hGSTA1-1 is a homodimer, there are two spin labeling sites, one in each monomer. The WE MD simulations focused on the wild-type enzyme.

3.1 | EPR distance distributions reveal an alternate ligand-free state

To characterize the conformational ensemble of the ligand-free hGSTA1-1 protein and any metastable states that result upon binding the GSHex substrate ligand, we performed a series of DEER experiments on the labeled hGSTA1-1 samples. Each sample was titrated with different hGSTA1-1:GSHex concentration ratios. For these experiments, the samples contained 100 μM hGSTA1-1 and a GSHex concentration of 0, 50, 100, 150, 200, and 400 μM. Note that a GSHex concentration of 200 μM nominally corresponds to a fully loaded protein with two GSHex available for the two binding sites, one in each monomer. For each sample, the specific binding of Cu(II)–NTA to dHis sites was verified by CW-EPR and ESEEM (Mims, 1972a, 1972b) experiments. These results are shown in Figures S1 and S2.

Next, DEER experiments were performed to measure the Cu(II)–Cu(II) distance distribution. The primary DEER time-domain signals are presented as black solid lines in Figure 2a. The primary DEER signal for each sample was performed at Q-band frequency (~34 GHz) and averaged over measurements at three optimal magnetic fields. The averaged DEER time-domain signal properly accounts for all molecular orientations and thus mitigates negative effects of orientational selectivity
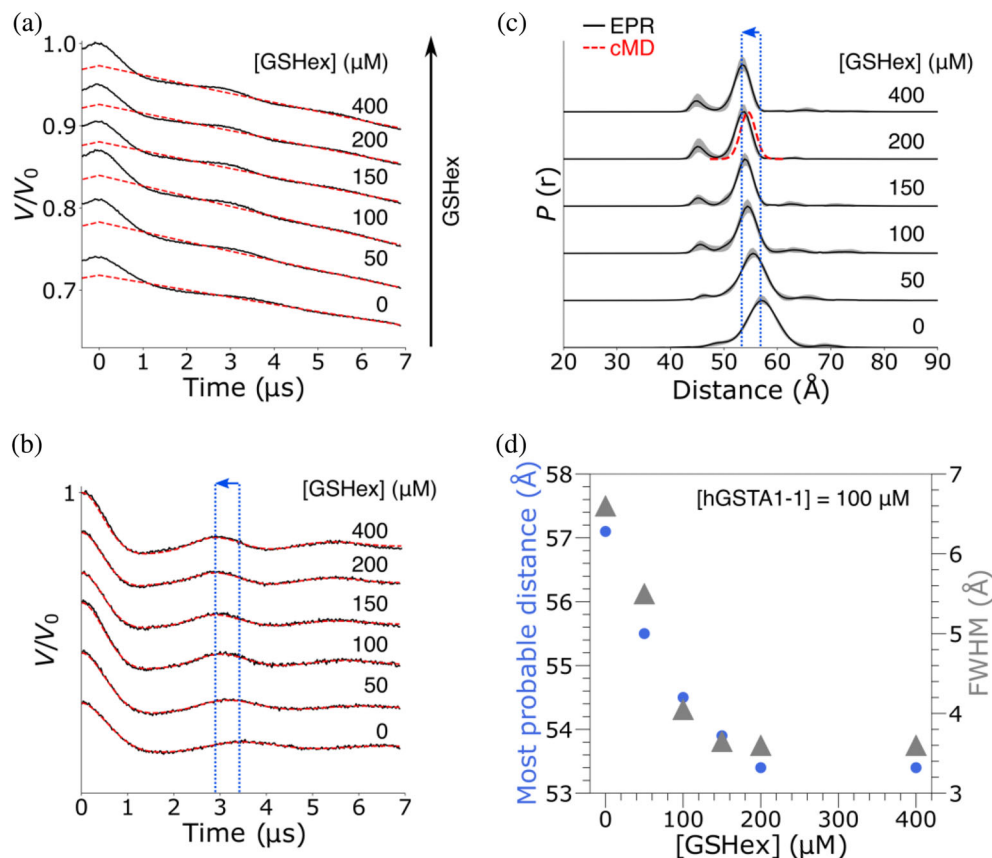
FIGURE 2 Q-band double electron–electron resonance (DEER) results for double histidine–Cu(II)–nitrilotriacetic acid bound human glutathione S-transferase A1-1 (hGSTA1-1) with different concentrations of S-hexylglutathione (GSHex) ligand. hGSTA1-1 concentration is 100 μM. (a) The solid, black curves show the primary DEER time-domain signals with increasing amount of GSHex ligand. The background signal is shown as dashed, red curves. The DEER signals were collected and averaged over three optimally positioned magnetic fields to account for all possible orientations of the hGSTA1-1 dimer. (b) The black curves show the background-subtracted DEER time trace corresponding to (a), with the Tikhonov fit shown using red dashed lines. The modulation periods shorten with GSHex concentration, as indicated by the arrow between the two vertical lines, and plateaus once one equivalent of GSHex is added. (c) Resulting distance distribution at each GSHex concentrations. The uncertainty is shaded in gray. With more ligand present, the most probable distance shifts from ∼57.1 to ∼53.4 Å, and the full width at half maximum (FWHM) decreases from ∼6.7 to ∼3.6 Å. Based on the GSHex-bound crystal structure (PDB:1K3L), the expected Cu(II)–Cu(II) distance is 53.6 Å. For direct comparison, the cMD sampled Cu(II)–Cu(II) distance distribution in the GSHex-bound form is plotted as red dashed line. (d) The trend in the most probable distance, shown as blue dots, and FWMH values, shown as gray triangles, at each GSHex concentration.

normally observed for measurements at Q-band (Bogetti et al., 2022). The background subtracted DEER signals are shown in Figure 2b. The signals, even in the complete absence of ligand, show clear modulations. Thus, we can conclude that α9 helix in the ligand-free hGSTA1-1 is likely folded. With increasing GSHex concentration from 0 to 200 μM, the modulation period shifted from 3.4 to 2.9 μs, which indicates that the most probable Cu(II)–Cu (II) distance decreased as more GSHex was added. The modulation of the DEER signals also became more resolved with the addition of GSHex ligand, indicating a narrowing of the distance distribution.

To extract the distance distributions, we applied the comparative DEER analyzer (Fábregas Ibáñez et al., 2020; Worswick et al., 2018) to the time traces. The resulting distributions are shown in Figure 2c. In the ligand-free state, a broad EPR distance distribution that ranges from ca. 45 to 65 Å is observed, which suggest that the α9 helix samples a wide range of conformations. With increasing GSHex ligand concentration, the distribution narrows, and the most probable distance shifts to lower distances. The most probable distance shows a maximum decrease of around 4 Å, as function of added GSHex ligand. This result indicates there is a subtle, yet noticeable difference in the most probable arrangement of the α9 helix in the ligand-free state versus the ligand-bound states.

We observed a gradual (non-discrete) shift and narrowing of the distance distribution with increasing GSHex ligand concentration (Figures 2c,d). In particular,

the most probable distance and full width at half maximum (FWHM) decreased significantly with increasing ligand concentration up to 100 µM at which point only half of the possible binding sites are occupied. Beyond this concentration and up to 200 µM, the most probable distance and FWHM continued to decrease, but more slowly. Although the shift and narrowing of the distance distribution was observed with increasing ligand concentration, the modulation depth across all samples remained mostly the same ($2.5\% \pm 0.4\%$).

To further explore the conformational changes of the hGSTA1-1 enzyme in the presence of different product ligands, we prepared hGSTA1-1 with EASG and GS-DNB. Such experiments are important given the high substrate promiscuity of hGSTA1-1. The Cu(II)–NTA loading for these samples were verified through CW-EPR and ESEEM experiments detailed in Figure S3. The primary DEER signals are shown in Figure S7. Interestingly, we observed similar distance distributions between Cu(II)–NTA labels in the GS-DNB- and GSHex-bound samples; in the EASG-bound sample, the distribution was broader with a longer, most probable distance (Figure 3). The EASG is a larger ligand compared to GS-DNB and GSHex, which brings the two α9 helices to a more open state as suggested in previous work (Cameron et al., 1995; Nilsson et al., 2002; Wang et al., 2000). The variation in the EPR distance distributions among these ligands provides us with further evidence that the α9 helices in hGSTA1-1 populate a broad range of conformations, and the relative positions of the two α9 helices are different in the ligand bound versus the ligand-free states. Furthermore, they suggest that conformational sampling

is relatively independent of the nature of the glutathione adduct for this enzyme. There is a minor peak around 45 Å in the distance distribution and possible interpretation for this peak is provided in the Supporting Information and Figure S6.

3.2 | Weighted ensemble MD generates direct views of negative cooperativity in the ligand-free ensemble

We found that the conformational transition from the ligand bound to the ligand-free state is inaccessible to cMD simulations. These results, shown in Figures 2c and S8–S13, are unsurprising given that this transition is expected to occur on the seconds-timescale (Nieslanik et al., 2001; Pettersson et al., 2017). Therefore, we performed WE simulations to focus MD simulation time on the transition rather than the stable state. Based on our EPR results, we chose a one-dimensional progress coordinate consisting of the heavy-atom RMSD of both α9 helices after aligning the rest of the dimer in the crystal structure (PDB:1K3L; see Section 2). Continuous pathways from the ligand-bound to the ligand-free state were captured from our WE simulations. Figure 4a shows a scatter plot with the RMSD of $\alpha9_A$ (x-axis) versus the RMSD of $\alpha9_B$ (y-axis) during the course of the WE simulation. The color of each point represents the value of the helicity metric of $\alpha9_B$ (see Section 2 for how this metric is calculated).

We found that the RMSD of one α9 helix ($\alpha9_B$) increases dramatically which indicates that this helix is
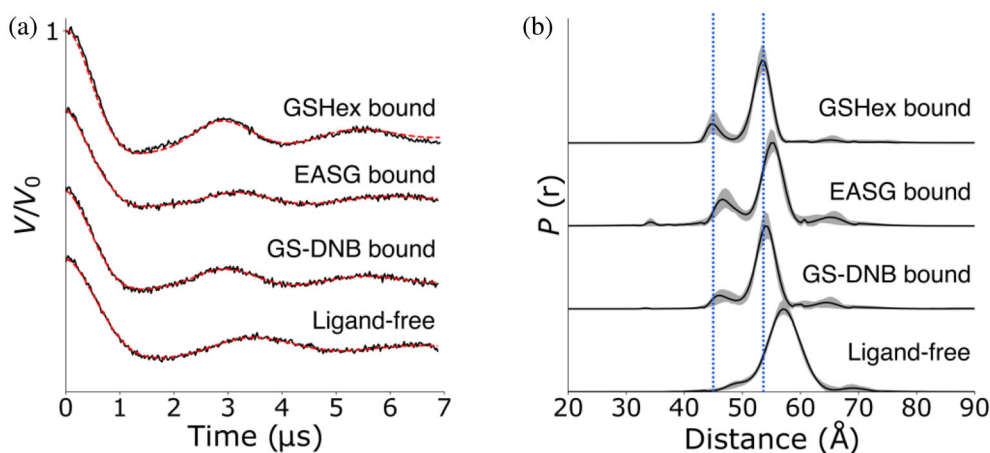
FIGURE 3 Comparison of Q-band double electron–electron resonance (DEER) results for double histidine–Cu(II)–nitrilotriacetic acid bound human glutathione S-transferase A1-1 (hGSTA1-1) without and with different ligands. (a) The black curves show the background-subtracted DEER time traces. The Tikhonov fit is shown by red lines. The ethacrynic acid glutathione conjugate (EASG) and S-(2,4-dinitrophenyl)glutathione (GS-DNB) bound samples contained five equivalents of ligand per hGSTA1-1 monomer to ensure ligand saturation of the binding sites. (b) The resulting distance distributions analyzed by DEERAnalysis21. The most probable distances of the major and minor distance populations for GSHex bound sample are labeled with vertical lines to aid comparison.
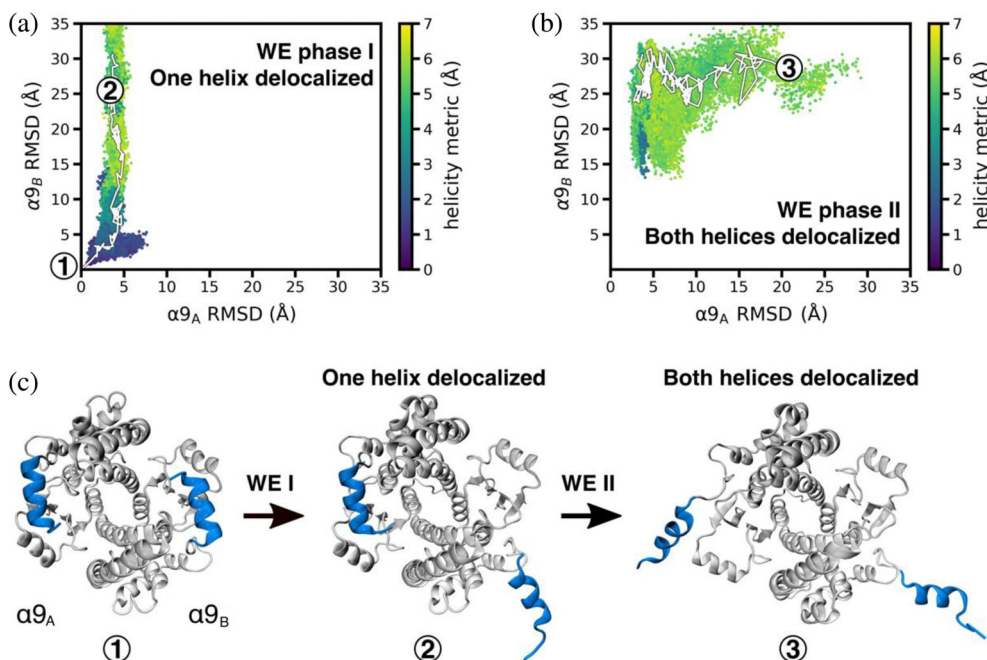
FIGURE 4 Combined EPR-weighted ensemble (WE) workflow was able to successfully generate atomically detailed conformations of human glutathione S-transferase A1-1 (hGSTA1-1) in the ligand-free state. (a) A scatter plot of all conformations sampled during this WE simulation as a function of (i) the heavy atom RMSD of $\alpha 9_A$ after aligning on the heavy atoms of the main body of the dimer and (ii) the heavy atom RMSD of $\alpha 9_B$ after aligning on the heavy atoms of the main body of the dimer. These RMSD metrics quantify the extent of delocalization for each helix. Each point in the scatter plot is colored according to a "helicity metric," that is, the heavy atom RMSD of $\alpha 9_B$ after aligning $\alpha 9_B$ to the heavy atoms of its initial structure, which indicates the extent to which $\alpha 9_B$ remains folded compared to its corresponding crystal structure conformation. In this first WE simulation, $\alpha 9_B$ was folded and delocalized while $\alpha 9_A$ did not delocalize to the same extent. A continuous pathway starting from the ligand-bound state (1) and ending in the ligand-free state (2) is traced as a white line. (b) Starting from the ligand-free state (2) in panel (a), where $\alpha 9_B$ was delocalized, a second WE simulation was run leading to conformations in which $\alpha 9_A$ also became delocalized. A scatter plot of all conformations generated during the second WE simulation is shown as a function of the same axes as the plot in panel (a) along with a continuous pathway leading to the delocalization of $\alpha 9_A$ (3) traced as a white line. (c) Snapshots of hGSTA1-1 in the ligand-bound state (1), with only $\alpha 9_B$ delocalized (2), and with both $\alpha 9_A$ and $\alpha 9_B$ delocalized (3) from our WE simulations, indicating a large extent of delocalization in the $\alpha 9$ helices (blue).

delocalized to a significant extent. In addition, the helicity metric value of $\alpha 9_B$ remains relatively low (around 2–3 Å) for most snapshots, which suggests that the helix stays folded and helical as it becomes delocalized. Surprisingly, while $\alpha 9_B$ delocalizes, the RMSD of the other helix ($\alpha 9_A$) does not increase at all, which suggests that this helix does not delocalize. A representative pathway for the conformational transition is traced in white, shown in Figure 4a, ending in the conformation labeled with 2. The shape of the RMSD distribution was even more surprising given that the progress coordinate used during the WE simulation to guide our sampling took the RMSD of *both* helices into account at the same time and given the homodimeric nature of the protein. We expected to observe simultaneous increases in the RMSD value of both helices. Instead, the WE results suggest a mechanism in which the undocking of one helix ($\alpha 9_B$) somehow prevents the undocking of the other (in this case, $\alpha 9_A$; see Movie S1). Replicates of this WE

simulation showed the same behavior, as well as a WE simulation run with a two-dimensional progress coordinate consisting of the RMSD of each helix, providing further support to our claims of negative cooperativity (Figure S14).

To delocalize both $\alpha 9$ helices in the ligand-free hGSTA1-1 enzyme, we initiated a second WE simulation from a conformation in which one helix is delocalized (shown as 2 in Figure 4a). For efficiency, we used a one-dimensional progress coordinate in this WE simulation consisting of the heavy-atom RMSD of only the $\alpha 9$ helix that is still localized ($\alpha 9_A$) after aligning the rest of the dimer in the crystal structure. This strategy was able to successfully delocalize the second helix. The RMSD values of each $\alpha 9$ helix for all trajectories from the second WE simulation are shown in Figure 4b. The coloring of each point here is consistent with Figure 4a. The need to apply a two-phase WE strategy suggests that once $\alpha 9_B$ has been fully delocalized, only then does the RMSD of

$\alpha 9_A$ increase, a finding consistent with the first WE simulation. Atomically detailed snapshot configurations from our WE simulation corresponding to the conformations 1-3 in Figure 4a,b, are plotted in Figure 4c.

Taken together, the WE simulation results indicate that the helices delocalize, one at a time, during the conformational transition to the ligand-free state. In addition, based on the helicity metric, and as easily visualized in Figure 4c and the Movie S1, both $\alpha 9$ helices stay mostly folded (helical) during the delocalization process. This latter finding supports some earlier work (Grahn et al., 2006; Nilsson et al., 2002; Pettersson et al., 2017; Zhan & Rule, 2004) and confirms a picture of the ligand-free ensemble in which a fully- or partially delocalized helix can interact with and potentially recruit ligands. Together, these results also demonstrate the remarkable potential of WE simulations to generate atomically detailed pathways for processes that occur on the seconds timescale. The first WE simulation generated 690 ns of total simulation time in 1.6 days using 16 NVIDIA A100 GPUs in parallel. The second WE simulation generated 309 ns of total simulation time in 16.8 h using 16 NVIDIA A100 GPUs in parallel.

Next, we verified that the conformations sampled from our WE simulations were stable states by selecting five conformations in which a *single* $\alpha 9$ helix in monomer B ($\alpha 9_B$) was delocalized and initiated a 1 μs cMD simulation from each conformation. The starting conformations are indicated by a star in Figure 5a. The distribution of all cMD-sampled conformations is plotted in Figure 5a as a function of the RMSD of each $\alpha 9$ helix. Each scatter point is colored according to the internal RMSD (foldedness) of $\alpha 9_B$. In all cMD simulations, both helices remain folded. Figure 5a reveals two populations: one in which a single $\alpha 9$ helix ($\alpha 9_B$) is only partly delocalized from its position in the ligand-bound crystal structure, and the other in which $\alpha 9_B$ is delocalized to a larger extent. This extent of helical delocalization in the ligand-free ensemble challenges previous speculation that both helices are completely delocalized (Nilsson et al., 2002; Pettersson et al., 2017). Here, we found that only one of the $\alpha 9$ helices is partly or fully delocalized yet the other $\alpha 9$ is well restricted. The dynamic nature of hGSTA1-1 and other enzymes in general has been previously suggested to potentially enable promiscuity (Nobeli et al., 2009). This statement is further supported by previous comparisons of the dynamics of hGSTA-1 and hGSTA4-4, which shows that the promiscuity is possibly enabled by conformational dynamics (Hou et al., 2007). Thus, delocalization of the $\alpha 9$ helices may promote searching for substrates.

To further investigate key interactions that control the delocalization of each $\alpha 9$ helix and any cooperativity due to these interactions, we analyzed a charged residue and hydrophobic interaction at the interface between the $\alpha 9$ helix and the rest of the protein. Previous studies have suggested the salt bridge (Widersten et al., 1996) and hydrophobic interactions (Nilsson et al., 2002) as being important for the stabilization of $\alpha 9$. However, the contribution of these interactions to the cooperativity between the monomers has not been discussed. Mutation of Phe220 to Ala or Thr has been shown to reduce the catalytic activity of hGSTA1-1 (Nilsson et al., 2002). In addition, mutation of a nearby residue of the Arg221/Asp42 bridge, Arg45 to Lys, has shown to decrease the catalytic activity of hGSTA1-1 toward 1-chloro-2,4-dinitrobenzene (CDNB). The authors concluded that the absence of the interaction between Arg45 and Arg42 may lead to the tightened salt bridge between Arg221/Asp42, which in turn may have resulted in the decrease in the catalytic activity against CDNB (Widersten et al., 1996). The Arg221/Asp42 salt bridge (Widersten et al., 1996) and Phe220/Phe10/Tyr9 hydrophobic interactions (Nilsson et al., 2002), which have been reported in the literature, are prominently featured in the cMD simulations initiated from WE sampled conformations. The Arg221/Asp42 and Phe220/Phe10 distances of one such simulation are plotted versus simulation time in Figure 5b (and Figure S15).

While $\alpha 9_B$ is delocalized, the Arg221/Asp42 interaction of $\alpha 9_A$, shown as the orange trace, stabilizes around 2.7 Å. Similarly, shown in light gray and dark gray traces in Figures 5b and S13, the aromatic–aromatic residue interactions provide another handle to stabilize the $\alpha 9_A$ while $\alpha 9_B$ is being delocalized. The charge–charge and hydrophobic interactions we identified in cMD simulations are represented as snapshots in Figure 5c,d. Interestingly, when taking all five cMD simulations of WE sampled conformations, we do not observe both helical Arg221/Asp42 interactions forming concurrently. These mutually exclusive salt-bridge interactions among the two monomers suggests negative cooperativity between the monomers. Additionally, we identified an additional, previously unreported salt-bridge interaction between Arg221/Glu39. These distances are shown in Figure S16. This additional salt bridge may further stabilize the $\alpha 9$ helix. The presence of these interactions likely leads to a ligand-free ensemble composed of many metastable states that are similar in energy, a known feature of the ligand-free ensemble of hGSTA1-1 (Nieslanik et al., 2001; Pettersson et al., 2017). These findings are consistent with biochemical studies that suggest negative cooperativity in a subset of GSTs (Bocedi et al., 2016; Lien et al., 2001), including A1-1, toward the toxic nitric oxide adduct, dinitrosyl-diglutathionyl iron (DNDGIC). In the case of some GSTs (glutathione S-transferase π family ofenzymes), the remaining active site remains catalytically functional, allowing the enzyme to both sequester
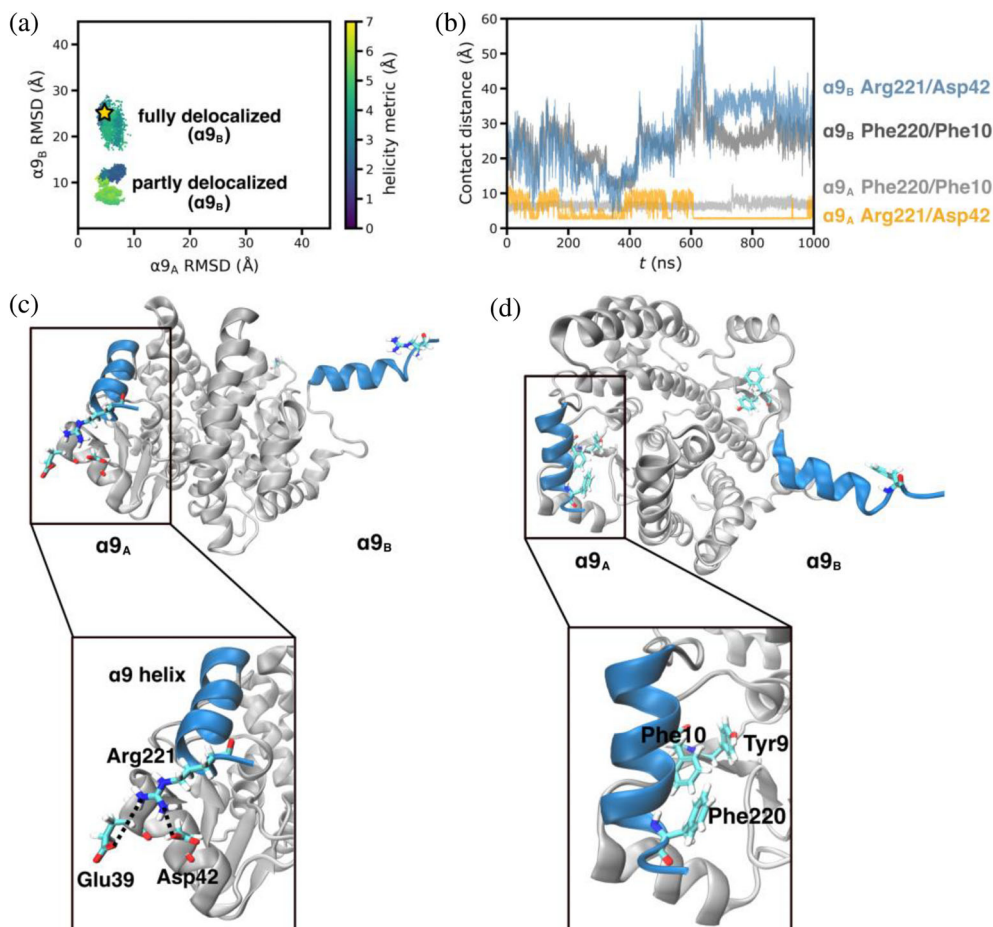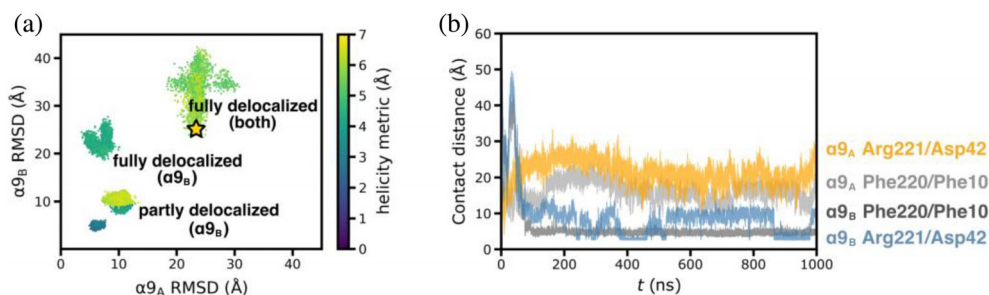
FIGURE 5 Conventional molecular dynamics (cMD) simulations started from human glutathione S-transferase A1-1 (hGSTA1-1) conformations extracted from our weighted ensemble (WE) simulations, confirm that we are sampling conformations within the ligand-free state. (a) All conformations sampled during the final 200 ns of five independent cMD simulations are plotted as a function of the heavy atom RMSD for each the two α9 helices after alignment on the heavy atoms of the main body of the dimer. Each cMD simulation was initiated from a hGSTA1-1 conformation sampled using WE (the gold star). The scatter points are colored according to the heavy atom RMSD (folded-ness) of the α9 helix of monomer B (α9$_B$) after aligning this helix to the heavy atoms in its initial structure. (b) Time-evolution of contacts between key interacting residues at the interface and either α9$_A$ or α9$_B$ based on a simulation with only α9$_B$ fully delocalized while α9$_A$ localized. These contacts are highlighted in snapshots from the cMD simulations in (c) and (d).

DNDGIC in one site and continue to detoxify in the other active site. However, in the case of A1-1, binding of DNDGIC leads to inactivation of the remaining active site. The cooperativity observed here may explain the behavior of the A1-1 enzyme in response to DNDGIC binding, in that the α9 helix in the empty monomer cannot productively localize over the active site.

To determine the extent to which states with both helices delocalized (undocked) are stable, we returned to the WE simulations and selected five conformations in which *both* α9 helices (α9$_A$ and α9$_B$) were delocalized at the same time. The initial states are represented by a star in Figure 6a. From each of these five conformations, we initiated 1 μs cMD simulations (Figure S17). Most conformations sampled in these cMD simulations settled into the wells that are similar to the ones shown in Figure 5a.

in which *only* α9$_B$ (and not α9$_A$) is partly or fully delocalized. Interestingly, one of these cMD simulations revealed an additional population where both α9 helices remained fully delocalized from the crystal structure of the ligand-bound conformation. Figure 6b shows the charged-residue distance between Arg221 and Asp42 from one of the cMD simulations where α9$_B$ is in the partly delocalized state. The charge–charge interaction has formed on α9$_B$, but not formed for α9$_A$, which provides further evidence of some sort of cooperativity within the hGSTA1-1 dimer. Similarly, the hydrophobic interaction between Phe220 and Phe10 keeps α9$_B$ stable around the binding site.

Combining the observed trend in the EPR distance distributions with the WE-sampled ligand-free conformations, we can conclude that both α9 helices remain at
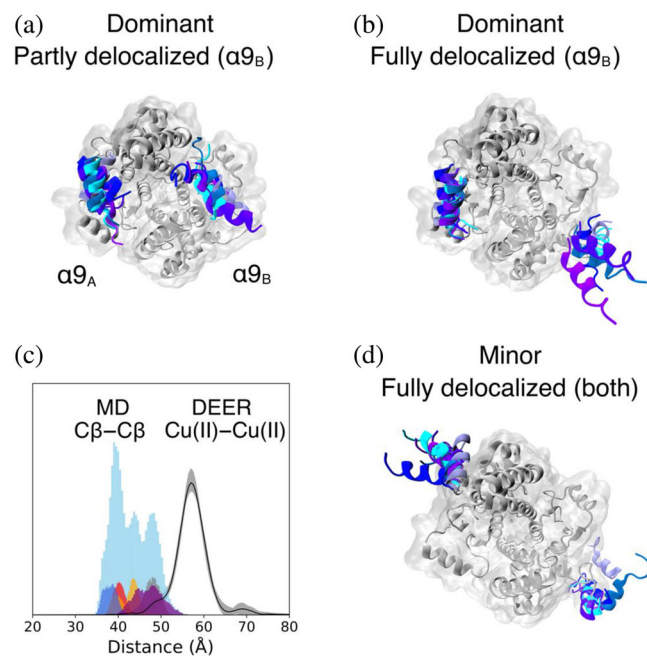
FIGURE 6 Additional conventional molecular dynamics (cMD) simulations, started from human glutathione S-transferase A1-1 conformations extracted from our weighted ensemble simulations in which both α9 helices were delocalized, further reveal the stable states of the ligand-free ensemble. (a) All conformations sampled during the final 200 ns of five independent cMD simulations are plotted as a function of the heavy atom RMSD values of each α9 helix after alignment on the heavy atoms of the main body of the dimer. The axes for this plot are the same as those in Figure 4a. We see much of the same stable conformations being formed during these cMD simulations, with the addition of a stable conformation in which both helices are delocalized to the same extent. The full 1 μs traces of these simulations, including where each started and ended, are provided in Figure S17. (b) The key interactions between the α9 helix and protein were plotted versus simulation time. The charge–charge distance of Arg221/Asp42 between $α9_A$ and protein is shown as an orange trace, and the corresponding interaction in $α9_B$ is shown as a blue trace. The hydrophobic interactions between Phe220/Phe10 of $α9_A$ are shown as a light gray trace and the corresponding interaction in $α9_B$ is shown as a dark gray trace. The Arg221/Asp42 interaction stabilizes $α9_B$ at a contact distance of around 2.7 Å, plotted as a blue trace. Meanwhile, the Phe220/Phe10 interaction seems to stabilize $α9_B$, with a contact distance around 5 Å.

least partially folded when delocalized (as evidenced by the relatively low values of the helicity metric of $α9_{A/B}$ compared to the corresponding values of the $α9_{A/B}$ RMSD values), and that only one helix delocalizes at a time. Shown in Figure 7, three populations of conformations best describe the ligand-free state: (1) one of the α9 helices remains localized while the other α9 helix is partly delocalized; (2) one of the α9 helices remains localized while the other one is completely delocalized; (3) a minor population with both of the α9 helices fully delocalized. The WE simulations portray a picture of the dominant mode in the ligand-free state consisting of one delocalized and mobile helix and one completely localized and immobile helix. The resulting Cβ–Cβ, defined here as the center of mass between the Cβ atoms of Lys211 and Glu215, distance distributions between $α9_A$ and $α9_B$ are shown in Figure 7c. The distribution in purple was sampled from a cMD simulation where only one α9 helix was fully delocalized, whereas the other distributions (in blue, red, gold, and gray) were sampled from the cMD simulations where only one α9 helix was partly delocalized. The overall distribution is shown in cyan. This broad Cβ–Cβ distribution corresponds well with the width of the EPR distance distribution, overlaid as a black curve and discussed above. This picture of controlled delocalization also rationalizes prior CW-EPR studies (Lawless et al., 2018; Singewald et al., 2020), which have consistently shown two-component spectra with different dynamics for the protein. In addition, a previous crystal structure of the ligand-free hGSTA1-1 (PDB: 1PKZ) shows partial electron density at one of the α9 (residues 210–219), yet the other α9 helix is mostly

unresolved in the diffraction data (Grahn et al., 2006). Such a scenario is consistent with a partly delocalized α9 helix such that only some residues are resolved in crystallography while the other helix is localized.

The delocalization of the α9 helices appears to be controlled by two charge–charge interactions as well as the hydrophobic interactions in hGSTA1-1 formed between the α9 and the hGSTA1-1 dimer. The conserved residues across many alpha class GSTs point to salt bridges and aromatic–aromatic interactions controlling the dynamics of the α9 helices. This controlled delocalization mechanism, in which many metastable states are separated by relatively small energy barriers explains the broad distance distribution of the ligand-free state measured by EPR (cf. Figures 2 and 3). More importantly, our WE simulations rationalize the trends in the distance distribution with increasing GSHex concentration (cf. Figure 2c,d). These data show a change in both the most probable distance and width of the distance distribution as a function of increasing ligand concentration. However, after half of the active sites are occupied with ligand, increasing ligand concentration resulted in smaller changes in the EPR distance distribution. Our WE results suggest a mechanism where only one monomer has a more flexible α9 helix. This monomer with a more flexible, delocalized α9 helix may initially bind to the ligand, locking that helix into place thereby shortening the most probable distance and narrowing the distance distribution. The other monomer with a localized helix may then be able to bind when all the binding sites with flexible, delocalized α9 helix are saturated. As such, the range of motions for this localized α9 helix is not significantly reduced due to

(a) Dominant
Partly delocalized (α9$_B$)

(b) Dominant
Fully delocalized (α9$_B$)

(c)

(d) Minor
Fully delocalized (both)

FIGURE 7 The weighted ensemble-molecular dynamics sampled ligand-free human glutathione S-transferase A1-1 conformations that best describe the EPR distance distribution. The conformations differ mainly at the α9 positions, with relative positions highlighted. The rest of the protein is shown in gray color. (a) Representative conformations with one α9 helix only partly delocalized from the crystal structure. (b) Representative conformations with one α9 helix fully delocalized from the crystal structure. (c) The distance distributions of the Cβ atoms (center of mass between the Cβ of Lys211 and Cβ of Glu215) between the two α9 helices within the dimer, compared to the double electron–electron resonance distance distribution in black. The purple distribution was sampled from a conventional molecular dynamics (cMD) simulation with one of the α9 fully delocalized conformations, while the other distributions (in blue, red, gold, and gray) were sampled from cMD simulations with partly delocalized α9 helix. The overall distribution is shown in cyan. (d) One of the cMD simulations sampled the conformations with both α9 helices completely delocalized from the crystal structure.

ligand binding such that the most probable distance remains mostly the same. Such negative cooperativity between the monomers may be essential to the recruitment of a wide variety of toxins within the cell during the process of toxin conjugation with glutathione. Figure 7 shows different conformations sampled in the ligand-free state that illustrate the wide variety of conformations that may constitute the EPR distance distribution.

4 | CONCLUSION

This work provides a deeper understanding of the ligand-free conformational ensemble of hGSTA1-1 at an atomic level using a combination of EPR experiments and WE simulations. Our EPR data shows that hGSTA1-1, and likely other structurally similar enzymes, exist in many interconvertible, metastable states. Ligand binding triggers a population shift among these metastable states, as indicated by a shift and narrowing of the EPR distance distribution. However, after half of the active sites are occupied with ligand, the EPR distance distribution exhibits much less change with increasing ligand concentration. Our WE simulations reveal three alternate states that are populated by the ligand-free form of hGSTA1-1. In the two dominant alternate states, the α9 helix is localized in one monomer whereas the α9 helix in the other monomer is delocalized. In the third minor alternate state, the α9 helix is delocalized in both monomers. Together, our EPR measurements and simulations provide direct atomistic views of negative cooperativity between the two monomers. Our simulations reveal a mutually exclusive salt bridge between Arg221 of the α9 helix and Asp42 of the α2 helix in each monomer of the hGSTA1-1 homodimer. We hypothesize that the mechanism governing this negative cooperativity involves these salt bridge interactions and does not result from the helices directly interacting with each other, but through some allosteric signal propagated through the main body of the dimer. Given that Arg221 is highly conserved across α-class GSTs, this mechanism of negative cooperativity may be general for such enzymes. Finally, our results demonstrate the power of combining EPR with WE sampling in providing mechanistic insights of protein function beyond the level of detail that is available using coarse-grained modeling approaches that are widely used in EPR (Jeschke, 2018).

CONFLICT OF INTEREST STATEMENT

The authors declare no conflicts of interests.

ORCID

Sunil Saxena https://orcid.org/0000-0001-9098-6114

REFERENCES

Abdullin D, Florin N, Hagelueken G, Schiemann O. EPR-based approach for the localization of paramagnetic metal ions in biomolecules. Angew Chem. 2015;127:1847–51.

Ackermann K, Wort JL, Bode BE. Nanomolar pulse dipolar EPR spectroscopy in proteins: Cu^{II}–Cu^{II} and nitroxide–nitroxide cases. J Phys Chem B. 2021;125:5358–64.

Altenbach C, Kusnetzow AK, Ernst OP, Hofmann KP, Hubbell WL. High-resolution distance mapping in rhodopsin reveals the pattern of helix movement due to activation. Proc Natl Acad Sci. 2008;105:7439–44.

Armstrong RN. Structure, catalytic mechanism, and evolution of the glutathione transferases. Chem Res Toxicol. 1997;10:2–18.

Barth K, Hank S, Spindler PE, Prisner TF, Tampé R, Joseph B. Conformational coupling and trans-inhibition in the human antigen transporter ortholog TmrAB resolved with dipolar EPR spectroscopy. J Am Chem Soc. 2018;140:4527–33.

Bocedi A, Fabrini R, Lo Bello M, Caccuri AM, Federici G, Mannervik B, et al. Evolution of negative cooperativity in glutathione transferase enabled preservation of enzyme function. J Biol Chem. 2016;291:26739–49.

Bogetti X, Ghosh S, Gamble Jarvi A, Wang J, Saxena S. Molecular dynamics simulations based on newly developed force field parameters for Cu^{2+} spin labels provide insights into double-histidine-based double electron–electron resonance. J Phys Chem B. 2020;124:2788–97.

Bogetti X, Hasanbasri Z, Hunter HR, Saxena S. An optimal acquisition scheme for Q-band EPR distance measurements using Cu^{2+}-based protein labels. Phys Chem Chem Phys. 2022;24: 14727–39.

Bonora M, Becker J, Saxena S. Suppression of electron spin-echo envelope modulation peaks in double quantum coherence electron spin resonance. J Magn Reson. 2004;170:278–83.

Borbat PP, Freed JH. Multiple-quantum ESR and distance measurements. Chem Phys Lett. 1999;313:145–54.

Cameron AD, Sinning I, L'Hermite G, Olin B, Board PG, Mannervik B, et al. Structural analysis of human alpha-class glutathione transferase A1-1 in the apo-form and in complexes with ethacrynic acid and its glutathione conjugate. Structure. 1995;3:717–27.

Casto J, Mandato A, Saxena S. dHis-troying barriers: deuteration provides a pathway to increase sensitivity and accessible distances for Cu^{2+} labels. J Phys Chem Lett. 2021;12:4681–5.

Chen VB, Arendall WB, Headd JJ, Keedy DA, Immormino RM, Kapral GJ, et al. *MolProbity*: all-atom structure validation for macromolecular crystallography. Acta Crystallogr D Biol Crystallogr. 2010;66:12–21.

Cunningham TF, Putterman MR, Desai A, Horne WS, Saxena S. The double-histidine Cu^{2+}-binding motif: a highly rigid, site-specific spin probe for electron spin resonance distance measurements. Angew Chem. 2015;127:6428–32.

Dalmas O, Sompornpisut P, Bezanilla F, Perozo E. Molecular mechanism of Mg2+-dependent gating in CorA. Nat Commun. 2014; 5:3590.

Dastvan R, Mishra S, Peskova YB, Nakamoto RK, Mchaourab HS. Mechanism of allosteric modulation of P-glycoprotein by transport substrates and inhibitors. Science. 2019;364:689–92.

Dirr HW, Wallace LA. Role of the C-terminal helix 9 in the stability and ligandin function of class α glutathione transferase A1-1. Biochemistry. 1999;38:15631–40.

Dommer A, Casalino L, Kearns F, Rosenfeld M, Wauer N, Ahn S-H, et al. #COVIDisAirborne: AI-enabled multiscale computational microscopy of delta SARS-CoV-2 in a respiratory aerosol. Int J High Perform Comput Appl. 2023;37:28–44.

Evans EGB, Morgan JLW, DiMaio F, Zagotta WN, Stoll S. Allosteric conformational change of a cyclic nucleotide-gated ion channel revealed by DEER spectroscopy. Proc Natl Acad Sci. 2020;117: 10839–47.

Evans EGB, Pushie MJ, Markham KA, Lee H-W, Millhauser GL. Interaction between prion protein's copper-bound octarepeat domain and a charged C-terminal pocket suggests a mechanism for N-terminal regulation. Structure. 2016;24:1057–67.

Fábregas Ibáñez L, Jeschke G, Stoll S. DeerLab: a comprehensive software package for analyzing dipolar electron paramagnetic resonance spectroscopy data. Magn Reson. 2020;1:209–24.

Gamble Jarvi A, Casto J, Saxena S. Buffer effects on site directed Cu2+-labeling using the double histidine motif. J Magn Reson. 2020;320:106848.

Gamble Jarvi A, Cunningham TF, Saxena S. Efficient localization of a native metal ion within a protein by Cu^{2+}-based EPR distance measurements. Phys Chem Chem Phys. 2019;21: 10238–43.

Gamble Jarvi A, Ranguelova K, Ghosh S, Weber RT, Saxena S. On the use of Q-band double electron–electron resonance to resolve the relative orientations of two double histidine-bound Cu^{2+} ions in a protein. J Phys Chem B. 2018;122:10669–77.

Ghosh S, Lawless MJ, Rule GS, Saxena S. The Cu2+-nitrilotriacetic acid complex improves loading of α-helical double histidine site for precise distance measurements by pulsed ESR. J Magn Reson. 2018;286:163–71.

Grahn E, Novotny M, Jakobsson E, Gustafsson A, Grehn L, Olin B, et al. New crystal structures of human glutathione transferase A1-1 shed light on glutathione binding and the conformation of the C-terminal helix. Acta Crystallogr D Biol Crystallogr. 2006;62:197–207.

Gustafsson A, Mannervik B. Benzoic acid derivatives induce recovery of catalytic activity in the partially inactive Met208Lys mutant of human glutathione transferase A1-1. J Mol Biol. 1999;288:787–800.

Hayes JD, Pulford DJ. The glutathione S-transferase supergene family: regulation of GST and the contribution of the isoenzymes to cancer chemoprotection and drug resistance part I. Crit Rev Biochem Mol Biol. 1995;30:445–520.

Hett T, Zbik T, Mukherjee S, Matsuoka H, Bönigk W, Klose D, et al. Spatiotemporal resolution of conformational changes in biomolecules by combining pulsed electron–electron double resonance spectroscopy with microsecond freeze-hyperquenching. J Am Chem Soc. 2021;143:6981–9.

Hirst SJ, Alexander N, Mchaourab HS, Meiler J. RosettaEPR: an integrated tool for protein structure determination from sparse EPR data. J Struct Biol. 2011;173:506–14.

Honaker MT, Acchione M, Zhang W, Mannervik B, Atkins WM. Enzymatic detoxication, conformational selection, and the role of molten globule active sites. J Biol Chem. 2013;288: 18599–611.

Hou L, Honaker MT, Shireman LM, Balogh LM, Roberts AG, Ng K, et al. Functional promiscuity correlates with conformational heterogeneity in A-class glutathione S-transferases. J Biol Chem. 2007;282:23264–74.

Huber GA, Kim S. Weighted-ensemble Brownian dynamics simulations for protein association reactions. Biophys J. 1996;70: 97–110.

Ibarra C, Nieslanik BS, Atkins WM. Contribution of aromatic−aromatic interactions to the anomalous pK_a of tyrosine-9 and the C-terminal dynamics of glutathione S-transferase A1-1. Biochemistry. 2001;40:10614–24.

Igarashi R, Sakai T, Hara H, Tenno T, Tanaka T, Tochio H, et al. Distance determination in proteins inside *Xenopus laevis* oocytes by double electron−electron resonance experiments. J Am Chem Soc. 2010;132:8228–9.

Islam SM, Stein RA, Mchaourab HS, Roux B. Structural refinement from restrained-ensemble simulations based on EPR/DEER data: application to T4 lysozyme. J Phys Chem B. 2013;117: 4740–54.

Izadi S, Anandakrishnan R, Onufriev AV. Building water models: a different approach. J Phys Chem Lett. 2014;5:3863–71.

Jeschke G. MMM: a toolbox for integrative structure modeling: a toolbox for integrative structure modeling. Protein Sci. 2018;27: 76–85.

Jeschke G, Chechik V, Ionita P, Godt A, Zimmermann H, Banham J, et al. DeerAnalysis2006—a comprehensive software package for analyzing pulsed ELDOR data. Appl Magn Reson. 2006;30:473–98.

Jeschke G, Pannier M, Godt A, Spiess HW. Dipolar spectroscopy and spin alignment in electron paramagnetic resonance. Chem Phys Lett. 2000;331:243–52.

Joseph B, Sikora A, Bordignon E, Jeschke G, Cafiso DS, Prisner TF. Distance measurement on an endogenous membrane transporter in *E. coli* cells and native membranes using EPR spectroscopy. Angew Chem. 2015;127:6294–7.

Kear JL, Blackburn ME, Veloro AM, Dunn BM, Fanucci GE. Subtype polymorphisms among HIV-1 protease variants confer altered flap conformations and flexibility. J Am Chem Soc. 2009;131:14650–1.

Krumkacheva OA, Shevelev GY, Lomzov AA, Dyrkheeva NS, Kuzhelev AA, Koval VV, et al. DNA complexes with human apurinic/apyrimidinic endonuclease 1: structural insights revealed by pulsed dipolar EPR with orthogonal spin labeling. Nucleic Acids Res. 2019;47:7767–80.

Kuhnert DC, Sayed Y, Mosebi S, Sayed M, Sewell T, Dirr HW. Tertiary interactions stabilise the C-terminal region of human glutathione transferase A1-1: a crystallographic and calorimetric study. J Mol Biol. 2005;349:825–38.

Kulik LV, Dzuba SA, Grigoryev IA, Tsvetkov YD. Electron dipole–dipole interaction in ESEEM of nitroxide biradicals. Chem Phys Lett. 2001;343:315–24.

Lawless MJ, Ghosh S, Cunningham TF, Shimshi A, Saxena S. On the use of the Cu^{2+}-iminodiacetic acid complex for double histidine based distance measurements by pulsed ESR. Phys Chem Chem Phys. 2017;19:20959–67.

Lawless MJ, Pettersson JR, Rule GS, Lanni F, Saxena S. ESR resolves the C terminus structure of the ligand-free human glutathione S-transferase A1-1. Biophys J. 2018;114:592–601.

Le Trong I, Stenkamp RE, Ibarra C, Atkins WM, Adman ET. 1.3-Å resolution structure of human glutathione S-transferase with S-hexyl glutathione bound reveals possible extended ligandin binding site: hGSTA1-1 with GTX. Proteins. 2002;48:618–27.

Lien S, Gustafsson A, Andersson A-K, Mannervik B. Human glutathione transferase A1-1 demonstrates both half-of-the-sites and all-of-the-sites reactivity. J Biol Chem. 2001;276:35599–605.

MacCallum JL, Perez A, Dill KA. Determining protein structures by combining semireliable data with atomistic physical models by Bayesian inference. Proc Natl Acad Sci. 2015;112:6985–90.

Marinelli F, Faraldo-Gómez JD. Ensemble-biased metadynamics: a molecular simulation method to sample experimental distributions. Biophys J. 2015;108:2779–82.

Martorana A, Bellapadrona G, Feintuch A, Di Gregorio E, Aime S, Goldfarb D. Probing protein conformation in cells by EPR distance measurements using Gd^{3+} spin labeling. J Am Chem Soc. 2014;136:13458–65.

Meichsner SL, Kutin Y, Kasanmascheff M. In-cell characterization of the stable tyrosyl radical in *E. coli* ribonucleotide reductase using advanced EPR spectroscopy. Angew Chem. 2021;133: 19304–10.

Milikisyants S, Scarpelli F, Finiguerra MG, Ubbink M, Huber M. A pulsed EPR method to determine distances between paramagnetic centers with strong spectral anisotropy and radicals: the dead-time free RIDME sequence. J Magn Reson. 2009;201: 48–56.

Milov AD, Maryasov AG, Tsvetkov YD. Pulsed electron double resonance (PELDOR) and its applications in free-radicals research. Appl Magn Reson. 1998;15:107–43.

Mims WB. Envelope modulation in spin-echo experiments. Phys Rev B. 1972a;5:2409–19.

Mims WB. Amplitudes of superhyperfine frequencies displayed in the electron-spin-echo envelope. Phys Rev B. 1972b;6:3543–5.

Nieslanik BS, Ibarra C, Atkins WM. The C-terminus of glutathione S-transferase A1-1 is required for entropically-driven ligand binding. Biochemistry. 2001;40:3536–43.

Nilsson LO, Edalat M, Pettersson PL, Mannervik B. Aromatic residues in the C-terminal region of glutathione transferase A1-1 influence rate-determining steps in the catalytic mechanism [Biochimica et Biophysica Acta 1597 (2002) 157–163]. Biochim Biophys Acta. 2002;1598:199–205.

Nobeli I, Favia AD, Thornton JM. Protein promiscuity and its implications for biotechnology. Nat Biotechnol. 2009;27: 157–67.

Nyenhuis DA, Nilaweera TD, Niblo JK, Nguyen NQ, DuBay KH, Cafiso DS. Evidence for the supramolecular organization of a

bacterial outer-membrane protein from in vivo pulse electron paramagnetic resonance spectroscopy. J Am Chem Soc. 2020; 142:10715–22.

Oranges M, Wort JL, Fukushima M, Fusco E, Ackermann K, Bode BE. Pulse dipolar electron paramagnetic resonance spectroscopy reveals buffer-modulated cooperativity of metal-templated protein dimerization. J. Phys Chem Lett. 2022;13: 7847–52.

Pannier M, Veit S, Godt A, Jeschke G, Spiess HW. Dead-time free measurement of dipole–dipole interactions between electron spins. J Magn Reson. 2011;213:316–25.

Park S-Y, Borbat PP, Gonzalez-Bonet G, Bhatnagar J, Pollard AM, Freed JH, et al. Reconstruction of the chemotaxis receptor–kinase assembly. Nat Struct Mol Biol. 2006;13:400–7.

Pettersson JR, Lanni F, Rule GS. Dual lifetimes for complexes between glutathione-S-transferase (hGSTA1-1) and product-like ligands detected by single-molecule fluorescence imaging. Biochemistry. 2017;56:4073–83.

Ploemen JHTM, van Ommen B, van Bladeren PJ. Inhibition of rat and human glutathione S-transferase isoenzymes by ethacrynic acid and its glutathione conjugate. Biochem Pharmacol. 1990; 40:1631–5.

Roser P, Schmidt MJ, Drescher M, Summerer D. Site-directed spin labeling of proteins for distance measurements in vitro and in cells. Org Biomol Chem. 2016;14:5468–76.

Russo JD, Zhang S, Leung JMG, Bogetti AT, Thompson JP, DeGrave AJ, et al. WESTPA 2.0: high-performance upgrades for weighted ensemble simulations and analysis of longer-timescale applications. J Chem Theory Comput. 2022;18: 638–49.

Ryckaert J-P, Ciccotti G, Berendsen HJC. Numerical integration of the cartesian equations of motion of a system with constraints: molecular dynamics of n-alkanes. J Comput Phys. 1977;23:327–41.

Saglam AS, Chong LT. Protein–protein binding pathways and calculations of rate constants using fully-continuous, explicit-solvent simulations. Chem Sci. 2019;10:2360–72.

Sameach H, Ghosh S, Gevorkyan-Airapetov L, Saxena S, Ruthstein S. EPR spectroscopy detects various active state conformations of the transcriptional regulator CueR. Angew Chem. 2019;131:3085–8.

Schiemann O, Heubach CA, Abdullin D, Ackermann K, Azarkh M, Bagryanskaya EG, et al. Benchmark test and guidelines for DEER/PELDOR experiments on nitroxide-labeled biomolecules. J Am Chem Soc. 2021;143:17875–90.

Schmidt T, Schwieters CD, Clore GM. Spatial domain organization in the HIV-1 reverse transcriptase p66 homodimer precursor probed by double electron-electron resonance EPR. Proc Natl Acad Sci. 2019;116:17809–16.

Schmidt T, Wang D, Jeon J, Schwieters CD, Clore GM. Quantitative agreement between conformational substates of holo calcium-loaded calmodulin detected by double electron–electron resonance EPR and predicted by molecular dynamics simulations. J Am Chem Soc. 2022;144:12043–51.

Schramm VL, McCluskey R, Emig FA, Litwack G. Kinetic studies and active site-binding properties of glutathione S-transferase using spin-labeled glutathione, a product analogue. J Biol Chem. 1984;259:714–22.

Singewald K, Bogetti X, Sinha K, Rule GS, Saxena S. Double histidine based EPR measurements at physiological temperatures permit site-specific elucidation of hidden dynamics in enzymes. Angew Chem Int Ed. 2020;59:23040–4.

Singewald K, Wilkinson J, Saxena S. Copper based site-directed spin labeling of proteins for use in pulsed and continuous wave EPR spectroscopy. Bio Protoc. 2021;11:e4258.

Stewart AM, Shanmugam M, Kutta RJ, Scrutton NS, Lovett JE, Hay S. Combined pulsed electron double resonance EPR and molecular dynamics investigations of calmodulin suggest effects of crowding agents on protein structures. Biochemistry. 2022;61:1735–42.

Stone KM, Townsend JE, Sarver J, Sapienza PJ, Saxena S, Jen-Jacobson L. Electron spin resonance shows common structural features for different classes of eco RI-DNA complexes. Angew Chem. 2008;120:10346–8.

Tesei G, Martins JM, Kunze MBA, Wang Y, Crehuet R, Lindorff-Larsen K. DEER-PREdict: software for efficient calculation of spin-labeling EPR and NMR data from conformational ensembles. PLoS Comput Biol. 2021;17:e1008551.

Teucher M, Zhang H, Bader V, Winklhofer KF, García-Sáez AJ, Rajca A, et al. A new perspective on membrane-embedded Bax oligomers using DEER and bioresistant orthogonal spin labels. Sci Rep. 2019;9:13013.

Tian C, Kasavajhala K, Belfon KAA, Raguette L, Huang H, Migues AN, et al. ff19SB: amino-acid-specific protein backbone parameters trained against quantum mechanics energy surfaces in solution. J Chem Theory Comput. 2020;16: 528–52.

Torrillo PA, Bogetti AT, Chong LT. A minimal, adaptive binning scheme for weighted ensemble simulations. J Phys Chem A. 2021;125:1642–9.

Wang J, Bauman S, Colman RF. Probing subunit interactions in alpha class rat liver glutathione S-transferase with the photoaffinity label glutathionyl S-[4-(succinimidyl)benzophenone]. J Biol Chem. 2000;275:5493–503.

Wang J, Wolf RM, Caldwell JW, Kollman PA, Case DA. Development and testing of a general amber force field. J Comput Chem. 2004;25:1157–74.

Widersten M, Björnestedt R, Mannervik B. Involvement of the carboxyl groups of glutathione in the catalytic mechanism of human glutathione transferase A1-1. Biochemistry. 1996;35: 7731–42.

Worswick SG, Spencer JA, Jeschke G, Kuprov I. Deep neural network processing of DEER data. Sci Adv. 2018;4:eaat5218.

Wort JL, Ackermann K, Norman DG, Bode BE. A general model to optimise Cu^{II} labelling efficiency of double-histidine motifs for pulse dipolar EPR applications. Phys Chem Chem Phys. 2021; 23:3810–9.

Wort JL, Arya S, Ackermann K, Stewart AJ, Bode BE. Pulse dipolar EPR reveals double-histidine motif Cu^{II}-NTA spin-labeling robustness against competitor ions. J Phys Chem Lett. 2021;12: 2815–9.

Yin DM, Hannam JS, Schmitz A, Schiemann O, Hagelueken G, Famulok M. Studying the conformation of a receptor tyrosine kinase in solution by inhibitor-based spin labeling. Angew Chem Int Ed. 2017;56:8417–21.

WILEY— THE PROTEIN SOCIETY

Zhan Y, Rule GS. Glutathione induces helical formation in the carboxy terminus of human glutathione transferase A1-1. Biochemistry. 2004;43:7244–54.

Zuckerman DM, Chong LT. Weighted ensemble simulation: review of methodology, applications, and software. Annu Rev Biophys. 2017;46:43–57.

SUPPORTING INFORMATION

Additional supporting information can be found online in the Supporting Information section at the end of this article.